





Article

Biomimetic Grooved Ribbon Aerogel Inspired by the Structure of *Pinus sylvestris* var. *mongolica* Needles for Efficient Air Purification

Bo Zhao ^{1,2,3}, Zikun Huang ², Mingze Han ^{1,2}, Bernardo Predicala ⁴ , Qiushi Wang ^{1,2}, Yunhong Liang ^{1,2} , Mo Li ^{1,2}, Xin Liu ^{1,2}, Jiangtao Qi ^{1,2,3,*}  and Li Guo ^{1,2,3,*} 

¹ Key Laboratory of Bionic Engineering, Ministry of Education of China, Jilin University, Changchun 130022, China; bozhao21@mails.jlu.edu.cn (B.Z.); hanmz22@mails.jlu.edu.cn (M.H.); wangqs22@mails.jlu.edu.cn (Q.W.); liangyunhong@jlu.edu.cn (Y.L.); moli@jlu.edu.cn (M.L.); lx2017@jlu.edu.cn (X.L.)

² College of Biological and Agricultural Engineering, Jilin University, Changchun 130022, China; huangzk9922@mails.jlu.edu.cn

³ Jilin Provincial Key Laboratory of Smart Agricultural Equipment and Technology, Changchun 130022, China

⁴ Prairie Swine Centre (PSC), Saskatoon, SK S7H 5N9, Canada; bernardo.predicala@usask.ca

* Correspondence: qjiangtao@jlu.edu.cn (J.Q.); liguo2012@jlu.edu.cn (L.G.)

Abstract: Air pollutants, such as particulate matter (PM) and ammonia (NH₃), generated by intensive animal farming pose considerable threats to human health, animal welfare, and ecological balance. Conventional materials are often ineffective at simultaneously removing multiple pollutants, maintaining a low pressure drop, and ensuring durability in heavily polluted environments. Inspired by the dust-retention properties of *Pinus sylvestris* var. *mongolica* (PS) needles, this study developed a biomimetic grooved ribbon fiber using electrospinning technology. These fibers were further assembled into a three-dimensional bioinspired aerogel structure through freeze-forming technology to achieve efficient dust capture. Additionally, the introduction of UiO-66-NH₂ nanoparticles significantly enhanced the properties of the aerogels for NH₃ adsorption. Among the various prepared aerogels (PG, UPG-5, UPG-10, UPG-15, and UPG-20), UPG-10 demonstrated the best performance, achieving a filtration efficiency of 99.24% with a pressure drop of 95 Pa. Notably, it exhibited a remarkable dust-holding capacity of 147 g/m², and its NH₃ adsorption capacity reached 99.89 cm³/g, surpassing PG aerogel by 31.46 cm³/g. Additionally, UPG-10 exhibited outstanding elasticity, maintaining over 80% of its original shape after 30 compression cycles. This biomimetic aerogel presents a promising solution for air purification, contributing to improved agricultural efficiency and environmental sustainability.

Keywords: electrospinning; grooved ribbon fiber; aerogel; air filtration; ammonia adsorption



Academic Editor: Iolanda De Marco

Received: 3 April 2025

Revised: 25 April 2025

Accepted: 28 April 2025

Published: 30 April 2025

Citation: Zhao, B.; Huang, Z.; Han, M.; Predicala, B.; Wang, Q.; Liang, Y.; Li, M.; Liu, X.; Qi, J.; Guo, L.

Biomimetic Grooved Ribbon Aerogel

Inspired by the Structure of *Pinus*

sylvestris var. *mongolica* Needles for

Efficient Air Purification. *Polymers*

2025, 17, 1234. <https://doi.org/10.3390/polym17091234>

Copyright: © 2025 by the authors.

Licensee MDPI, Basel, Switzerland.

This article is an open access article

distributed under the terms and

conditions of the Creative Commons

Attribution (CC BY) license

(<https://creativecommons.org/licenses/by/4.0/>).

1. Introduction

Air pollutants emitted from intensive animal farming are significantly different from those commonly found in the atmosphere [1]. These pollutants originate from complex sources such as feces, dander, urine, feed, skin, and hair, which disperse into the air and generate significant microbial aerosols [2]. In this highly polluted environment, particulate matter (PM) is not the only concern, as heavy metals, toxic gases, and microorganisms can also pose health risks by entering the body. [3]. Among these pollutants, PM and ammonia (NH₃) are the most prominent. Studies have indicated that chronic exposure to PM is a significant factor in the development of respiratory conditions, such as pneumonia and

bronchitis. [4]. Furthermore, high concentrations of NH_3 may cause serious damage to the eyes, nose, and skin [5]. These pollutants not only pose a threat to workers and animals in the facility, but can also be released into the external environment through ventilation systems, contributing to the deterioration of regional air quality.

To effectively mitigate the pollutants in animal facilities, improving the ventilation efficiency of animal facilities is a crucial step. This requires installing advanced ventilation systems and utilizing suitable filter materials that can significantly lower pollutant levels, thus mitigating negative health impacts on both animals and workers [6]. Currently, activated carbon and glass fibers are the primary filter materials used for air purification in animal-rearing environments [7]. Activated carbon is widely employed for its large surface area and strong adsorption capacity, making it highly effective in capturing NH_3 and volatile organic compounds (VOCs) [8]. Glass fibers, on the other hand, are valued for their structural durability and are primarily used to physically block bacteria and trap larger airborne particles. However, it is difficult for these materials to simultaneously capture PM and adsorb NH_3 [9–11]. Additionally, due to the high concentration of pollutants in animal facilities, it is also essential to have sufficient dust-holding capacity (DHC) in addition to fulfilling basic filtering requirements. Filters with high DHC can more effectively extend the service life of the filtration system, reducing the frequency of maintenance and replacement, and reducing operating costs [12]. Therefore, developing an integrated filter material capable of simultaneously achieving all these functions represents a significant challenge for both the research community and industry practitioners.

Aerogels are one of the most attractive materials, with ultra-low density, minimal pore size, and high porosity, making them highly suitable for air purification [13,14]. The filtration performance of aerogels is significantly influenced by their morphological structure. For example, Qiao et al. (2020) enhanced air permeability and maintained over 99.8% filtration efficiency by incorporating polyvinylidene fluoride (PVDF) into a 3D crosslinked polyimide (PI) network [15]. Su et al. (2024) fabricated an oxidized “grooved and secondary pore”-structured polyaryl thioether sulfone (O-GPPASS) aerogel, achieving $\text{PM}_{0.3}$ filtration efficiency for 99.7% and a low pressure drop of 17.2 Pa [16]. Moreover, compared with two-dimensional filtration media, aerogels’ three-dimensional structures enable them to capture more particles, substantially increasing dust-holding capacity and extending the lifespan of filtration materials [12,17,18]. Aerogels integrated with metal–organic frameworks (MOFs) further enhance gas adsorption capabilities, demonstrating effectiveness in capturing formaldehyde, methane, carbon dioxide, and hydrogen sulfide [10,19–23]. Notably, diverse functionalized variants of UiO-66, especially UiO-66- NH_2 , exhibit exceptional NH_3 removal performance in environments [24–26]. However, despite these advancements demonstrating the potential of aerogels, existing studies often focus on optimizing either PM filtration efficiency or gas adsorption. Therefore, developing aerogels that perform exceptionally in both aspects remains a significant challenge.

In nature, needles of the *Pinus sylvestris* var. *mongolica* Litv. (PS) exhibit unique structural advantages for dust retention. Their groove structures increase the specific surface area, enhancing their effectiveness in intercepting PM. Additionally, the irregular arrangement of the needles effectively reduces air resistance. When dust-laden airflow passes through PS, these varying orientations generate vortices that efficiently capture particulates while maintaining low airflow resistance. Based on this phenomenon, and combined with the exceptional adsorption capabilities of UiO-66- NH_2 nanoparticles, we developed a high-performance biomimetic aerogel in this study. The research focuses on two primary objectives: (1) optimizing fiber structures by adjusting the polylactic acid (PLA)-to-gelatin ratio during the electrospinning process to prepare biomimetic fibers, and (2) incorporating UiO-66- NH_2 nanoparticles into these fibers, utilizing freeze-drying technology to assemble

one-dimensional fiber into three-dimensional aerogels with low airflow resistance and efficient NH_3 adsorption. The filtration efficiency, dust-holding capacity, NH_3 adsorption performance, and elasticity of the developed aerogel were systematically evaluated. These assessments aimed to establish whether this innovative material represents a viable solution for air purification in heavily polluted environments. Furthermore, this work aimed to contribute to advancing biomimetic filtration technologies, supporting both industrial pollution control efforts and environmental sustainability initiatives.

2. Materials and Methods

2.1. Materials

Zirconium chloride (ZrCl_4 , 98%), 2-amino-1,4-dicarboxylic acid (BDC-NH_2 , 98%), poly (lactic acid) (PLA, $M_W = 110,000$), 1,1,1,3,3,3-hexafluoro-2-propanol (HFIP, 99.5%), and *N,N*-dimethylformamide (DMF, AR, $\geq 99.5\%$) were obtained from Shanghai Macklin Biochemical Co., Ltd. (Shanghai, China). Gelatin (Type A) was provided by Shanghai yuanye Bio-Technology Co., Ltd. (Shanghai, China). Tert-Butyl alcohol was obtained from Tianjin Xinbote Chemical Co., Ltd. (Tianjin, China). Methanol was bought from Tianjin Fuyu Fine Chemical Co., Ltd. (Tianjin, China).

2.2. Fabrication of Biomimetic Fibers

The preparation of the biomimetic fibers was undertaken as follows: first, PLA was dissolved in HFIP to prepare 5 wt% PLA solution and stirred at 60 °C for 3 h. At the same time, gelatin was dissolved in HFIP to prepare 8 wt% gelatin solution, and this mixture was also stirred at 60 °C for 3 h. Then, the PLA and gelatin solutions were mixed at PLA and gelatin mass ratios of 6:0, 5:1, 4:2, 3:3, 2:4, 1:5, and 0:6, and stirred to obtain solutions in a homogeneous state. These various solutions were fed to the electrospinning machine (Elite, Beijing Ucalery Technology and Development Co., Ltd., Beijing, China) with a positive voltage of 15 KV, voltage pressure of 5 KV, flow rate of 1.5 mL/h, and distance between the spinneret and the collector of 15 cm, to obtain membranes labelled as P6, P5G1, P4G2, P3G3, P2G4, P1G5, G6, respectively.

2.3. Fabrication of UiO-66-NH_2 @PLA/Gelatin Nanofibrous Aerogels

The synthesis of UiO-66-NH_2 nanoparticles was carried out in accordance with the method detailed in a previous publication [27,28]. Figure 1a shows the preparation process of the aerogels. Firstly, the P1G5 nanofiber membrane was cut into small pieces of about $1 \text{ cm} \times 1 \text{ cm}$, and 0.4 g of P1G5 nanofibers were put into 20 mL of tert-butyl alcohol. Then the mixture was uniformly ultrasonicated at 600 W for 2 min with an ultrasonic cell crusher (SCIENTZ-IIID, Ningbo Xinzhi Biotechnology Co., Ltd., Ningbo, China). Meanwhile, different amounts of UiO-66-NH_2 at 0, 0.02, 0.04, 0.06, and 0.08 g were homogeneously dispersed into 20 mL of tert-butyl alcohol, then added into the P1G5 nanofibers/tert-butyl alcohol mixture and homogeneously dispersed again by an ultrasonic cell crusher. Next, 10 mL of the above homogeneous nanofiber mixtures were poured into 38.5 mm diameter molds and cooled to $-30 \text{ }^\circ\text{C}$ for 12 h. The samples were subsequently freeze-dried in a freeze-dryer (SCIENTZ-12N, Ningbo Xinzhi Biotechnology Co., Ltd., Ningbo, China) for 24 h. Finally, the obtained 3D aerogels were cross-linked in a muffle furnace (MF-1700C-II, Anhui BeiYiKe Equipment Technology Co., Ltd., Hefei, China) at 140 °C for 2 h. The obtained aerogel samples were labelled as PG, UPG-5, UPG-10, UPG-15, and UPG-20, according to UiO-66-NH_2 content relative to P1G5 nanofibers (0%, 5%, 10%, 15%, and 20%). Additionally, pure PLA aerogel and Gelatin aerogel were prepared using P6 nanofiber and G6 nanofiber and used as reference. Figure 1b shows the schematic diagram of air purification with UPG aerogels.

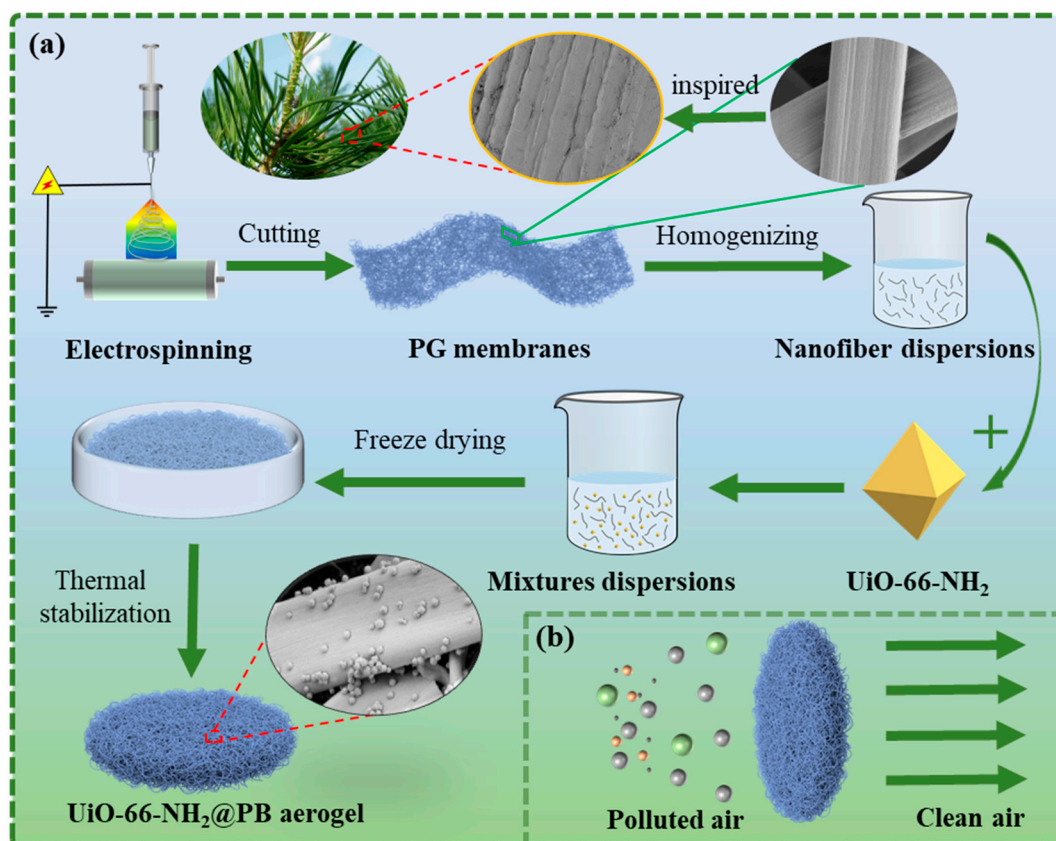


Figure 1. Schematic illustration of the preparation process (a) and use for filtration (b) of bionic UPG aerogels.

2.4. Characterization

A scanning electron microscope (SEM) (Su-70, Hitachi, Tokyo, Japan) was used to characterize the morphologies of the prepared membranes and aerogels. The X-ray diffraction patterns of the samples were analyzed using XRD (6100, Shimadzu, Kyoto, Japan), while sample chemical compositions were determined using FT-IR (iS50, Thermo Nicolet Corporation, Madison, WI, USA). The surface chemical states and elemental compositions were examined using XPS (Escalab250Xi, ThermoFisher, Waltham, MA, USA), and TGA/DTG (HTG-1, Henven, Beijing, China) was used to study the thermal stability of the aerogels under a N₂ atmosphere. N₂ adsorption desorption curves were measured using an advanced gas adsorption and micropore analyzer (BSD-660 M, BSD Instrument Inc., Beijing, China). The specific surface area and pore size distribution were analyzed using the BET methods and NLDFT methods. An automated gas sorption analyzer (Autosorb iQ, Quantachrome Instrument Inc., Boynton Beach, FL, USA) was used to analyze the NH₃ adsorption capacity.

2.5. Filtration Performance Measurement

The filtration performance was evaluated utilizing the test platform (Figure S1) with a controlled flow rate of 5.3 cm/s. The filtration efficiency of PM (µg/cm³) was calculated using Equation (1) [29]:

$$\eta(PM) = \frac{C_{up}(PM) - C_{down}(PM)}{C_{up}(PM)} \quad (1)$$

where $C_{up}(PM)$ and $C_{down}(PM)$ represent the upstream and downstream concentrations of PM_1 (particle sizes less than 1 μm), $PM_{2.5}$ (particle sizes less than 1 μm), and PM_{10} (particle sizes less than 1 μm), respectively.

To comprehensively assess the filtration performance, the quality factor (QF, Pa^{-1}) was calculated using Equation (2) [30]:

$$QF = \frac{-\ln(1 - \eta)}{\Delta P} \quad (2)$$

where ΔP (Pa) is the pressure drop of the tested membranes/aerogels.

The DHCs of the membranes/aerogels were measured using the same filter holder (Figure S1) under a flow rate of 10.6 cm/s. The measurement was terminated once the pressure drop of membranes/aerogels reached the preset industrial threshold of 1000 Pa. The DHCs of membranes/aerogels was calculated using Equation (3) [31]:

$$D = (M_t - M_0) / A \quad (3)$$

where M_t (g) and M_0 (g) are the mass of the aerogels with accumulated PM and the clean aerogels, respectively, and A (m^2) is the effective area of the aerogels. All tests were conducted at 25 ± 5 °C.

3. Results and Discussion

3.1. Characterization of Bionic Ribbon PLA/Gel Fiber Membrane

The physical morphology of nanofibers had an important influence on their filtration performance [32]. Conventional nanofibers, characterized by their smooth and bead-free structure, seem to be inadequate in terms of filtration performance owing to their conventional interception mechanisms [33]. In nature, PS has been identified as an effective approach to mitigate PM in the atmosphere, primarily due to the presence of numerous “grooved” stripes in the microstructure of its needles [34]. Figure 2a shows an optical photograph of PS, with the inset showing a 3D ultra-depth-of-field digital image of PS needles, which clearly reveals the striped grooves and pore bands on the needle surface. Additionally, the SEM image in Figure 2b highlights the prominent “grooved” structures on the PS needles. In this study, the structure and morphology of bionic grooved ribbon fibers were controlled by varying the PLA-to-gelatin mass ratio in the precursor solutions using electrospinning technology. As shown in Figure 2c, pure PLA nanofibers display a cylindrical shape with some small protrusions on the surface. With an increasing concentration of gelatin (from P5G1 to P3G3), the rod-like morphology of the nanofibers remains largely unaffected, while the surface protrusions become more pronounced, aligning in the direction of the fibers, as illustrated in Figure 2d–f. When the gelatin content exceeds that of PLA, the resulting fibers exhibit a cylindrical shape with long grooves, as shown in Figure 2g. Notably, P1G5 morphology shows ribbon-like fibers with distinct long grooves, forming a bionic nano-grooved ribbon fiber ranging from approximately 166 nm to 261 nm, as depicted in Figure 2h. Conversely, pure gelatin fibers exhibit a smooth ribbon-like morphology, as shown in Figure 2i. These results demonstrate that in the mixed solution system composed of PLA and gelatin, reducing the PLA content promotes the formation of vertical grooves on the fiber surface, while increasing gelatin content gradually transforms the morphology to ribbon-like fibers.

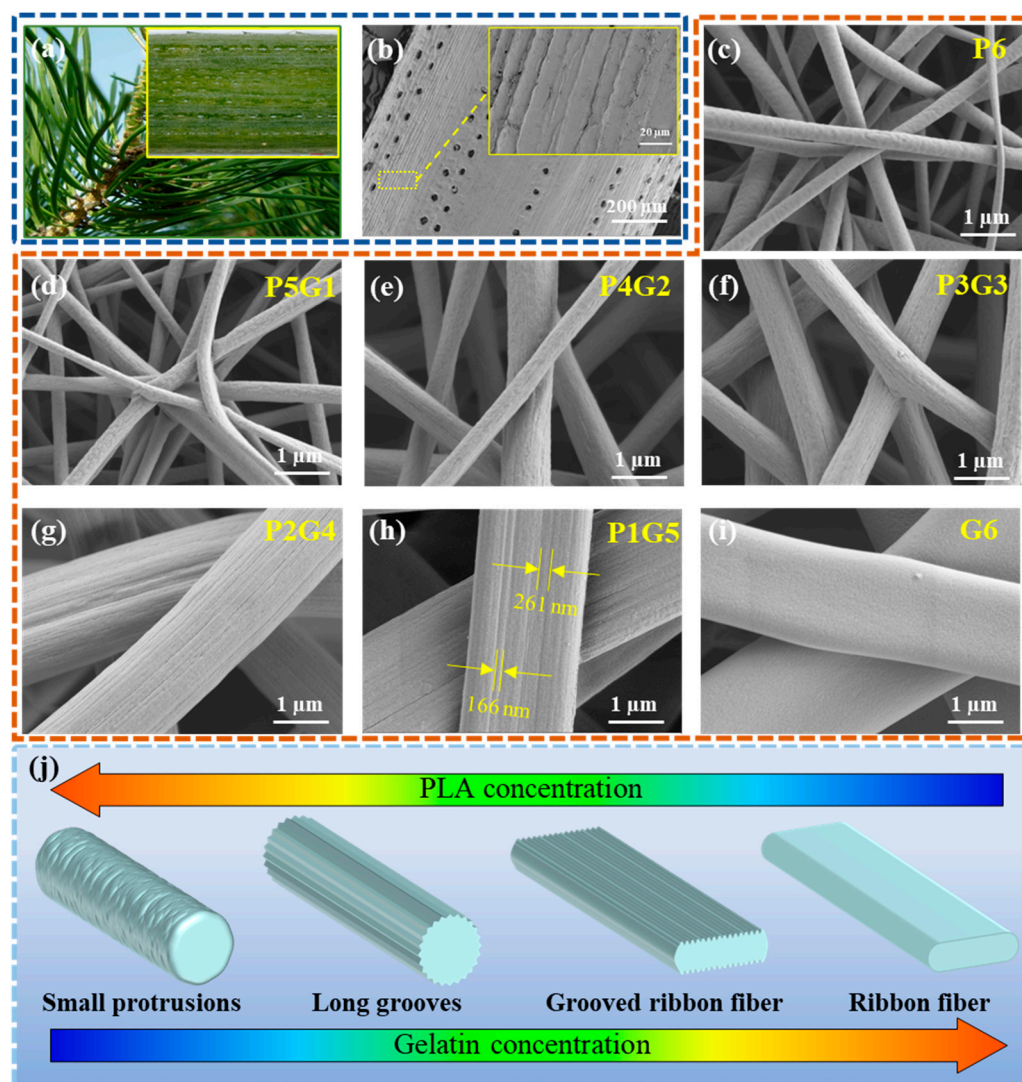


Figure 2. Characterization and formation mechanism of the bionic striped ribbon fibers. (a) Optical photograph and 3D ultra-depth-of-field digital photograph of PS; (b) SEM images of PS needles; SEM images of the (c) P6, (d) P5G1, (e) P4G2, (f) P3G3, (g) P2G4, (h) P1G5, and (i) G6 electrospun fibers; and (j) formation mechanism of the bionic striped ribbon fibers.

The formation mechanism of the bionic grooved ribbon fibers is further analyzed, as depicted in Figure 2j. In the mixed solution system, the heterogeneous evaporation of solvent plays a key role in forming the nano-grooved ribbon fiber morphology [33,35,36]. Firstly, the solution conductivity directly impacts the morphology of electrospun nanofibers [37]. The increased conductivity alters the electric field intensity and accelerates solvent evaporation, thereby affecting the formation of uniquely shaped fibers [38]. Compared to the pure PLA precursor, the addition of gelatin markedly improves the conductivity of the precursor solutions (Table 1), which promotes the formation of ribbon-like fibers during the electrospinning. Additionally, the concentration of gelatin serves as a key factor in controlling fiber morphology. As the gelatin concentration increases, the fibers develop longer grooves, gradually transitioning from rod-like to ribbon-like structures. The amino and carboxyl groups present in gelatin form hydrogen bonds with the hydroxyl or carboxyl groups in PLA, resulting in a cross-linked system. Higher gelatin content increases the degree of cross-linking, leading to enhanced polymer chain entanglement. Under these conditions, the solvent diffuses gradually from the interior of the jet to the surface, resulting in the formation of nano-grooved ribbon fibers.

Table 1. Conductivity of electrospinning precursors.

| Electrospinning Precursors | P6 | P5G1 | P4G2 | P3G3 | P4G2 | P5G1 | G6 |
|--|-------------------|-------------------|-------------------|-------------------|-------------------|-------------------|-------------------|
| Conductivity ($\mu\text{S cm}^{-1}$) | 0.031 ± 0.002 | 0.517 ± 0.002 | 0.707 ± 0.002 | 0.905 ± 0.001 | 1.168 ± 0.001 | 1.321 ± 0.002 | 1.528 ± 0.003 |

3.2. Characterization of PLA/Gel/MOF Nanofibrous Aerogels

The bionic nano-grooved ribbon fibers were subsequently used to prepare PG aerogels and UPG aerogels, with the latter doped with varying masses of UiO-66-NH₂. The SEM analysis of the synthesized UiO-66-NH₂ nanoparticles (Figure S2) confirmed that they have a distinctive octahedral morphology, consistent with established crystal structures reported in the literature [39,40]. The microstructures of aerogels with different UiO-66-NH₂ concentrations are presented in Figure 3a–e, revealing that all aerogels retain the same ribbon fiber morphology as the original PG nanofibers. With an increase in the concentration of UiO-66-NH₂ nanoparticles, a greater number of nanoparticles are observed on the ribbon fibers. Furthermore, the bionic nano-grooved ribbon fibers exhibit a randomly oriented arrangement within the three-dimensional aerogel, allowing both the main surfaces and the edges of the ribbon-like fibers to be visible. This multidirectional alignment contributes to reducing airflow resistance. As presented in Figure 3f (magnified view of UPG-10), the UiO-66-NH₂ was uniformly dispersed onto the surface of the ribbon fibers. EDS elemental mapping analysis of UPG-10 aerogel confirms the presence and uniform distribution of these elements (Figure 3g). Additionally, a piece of UPG-10 aerogel with a density of about $14.9 \pm 0.2 \text{ mg/cm}^3$ UPG-10 aerogel can be effortlessly placed onto the stamen of a flower, as shown in Figure 3h, highlighting its lightweight nature.

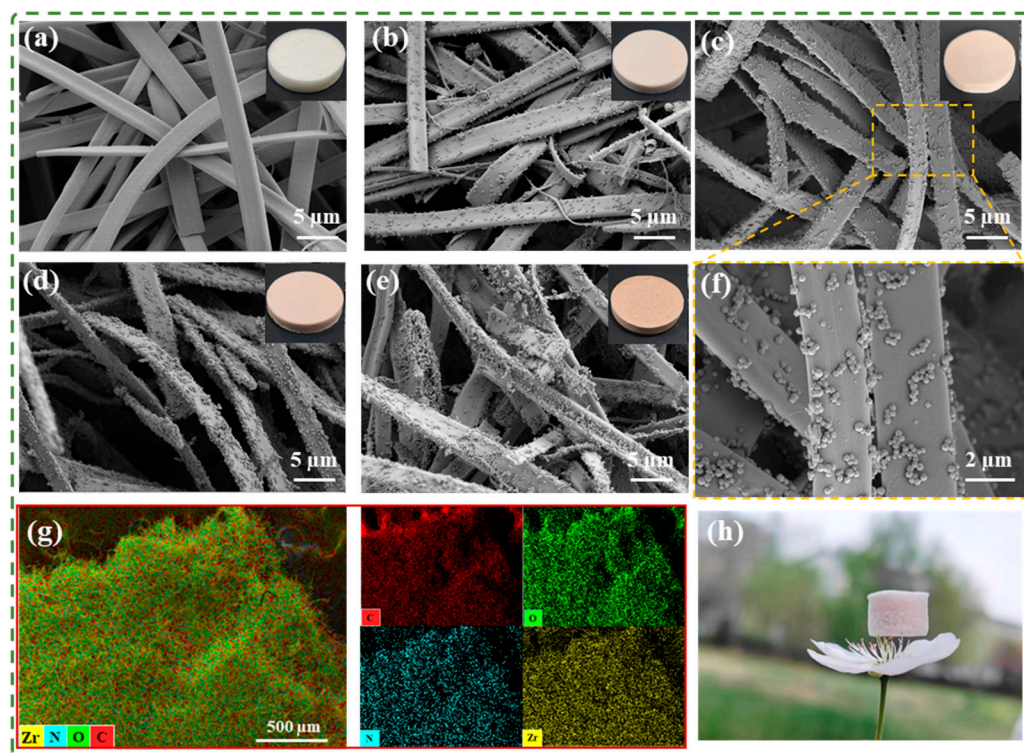


Figure 3. Morphological characterization of the aerogels. SEM of (a) PG, (b) UPG-5, (c) UPG-10, (d) UPG-15, (e) UPG-20, and the insets are their optical photographs. (f) Magnified view of UPG-10. (g) EDS elemental mapping image of the UPG-10 aerogel. (h) Optical photo of UPG-10 on the stamen of a flower.

To investigate the effect of doping concentration on PG aerogels, a series of UPG aerogels with different UiO-66-NH₂ contents were characterized. Figure 4a displays the XRD spectrum of the aerogels before and after mixing with UiO-66-NH₂. The peak at 20.6° for the PG sample can be attributed to the characteristic peak of gelatin, but the characteristic peak of PLA could not be seen, probably due to the low PLA content [41]. Typical strong diffraction peaks correspond to the (111) and (222) lattice planes of UiO-66-NH₂, respectively. The characteristic peaks of UiO-66-NH₂ were also observed in the diffraction patterns of the composite aerogels. Figure 4b presents the FTIR spectra of the UiO-66-NH₂, PG, and UPG aerogels. The characteristic absorption bands at approximately 620 cm^{−1} and 770 cm^{−1} are attributed to Zr-O bonds in UiO-66-NH₂ [42,43]. The peak at 3100–3600 cm^{−1} corresponds to the stretching vibration of O-H groups of PLA in the PG aerogel and UiO-66-NH₂, as well as the N-H stretching in the gelatin in the PG aerogel [44]. The peaks at 1644 cm^{−1} and 1536 cm^{−1} represent the amide I and amide II bands of the PG aerogel, respectively [44,45]. The peak at 1750 cm^{−1} is indicative of the -CHO stretching vibration in PLA, while the range from 2850 to 2950 cm^{−1} denotes the aliphatic C-H stretching found in both gelatin and PLA [46]. As shown in the survey spectrum of Figure 4c, UPG-x exhibits all elemental peaks of both PG and UiO-66-NH₂, including C 1s, N 1s, O 1s, and Zr 3d. An increase in UiO-66-NH₂ concentration enhances the intensities of C 1s and Zr 3d peaks while reducing those of O 1s and N 1s, reflecting a higher proportion of C and Zr elements and a lower proportion of O and N elements, which is consistent with the compositional data in Table S1. The high-resolution XPS spectrum for Zr 3d in UiO-66-NH₂/UPG-x features two distinct peaks at 185.23 eV and 182.84 eV for the 3d_{3/2} and 3d_{5/2} levels, respectively, consistent with those in pure UiO-66-NH₂, as depicted in Figure 4d. The characteristic peak intensity of UiO-66-NH₂ progressively increased as its loading ratio increased. Additionally, Figure S3 presents the high-resolution XPS spectra of C 1s, N 1s, O 1s, and Zr 3d over UPG-10 respectively [47–50]. The presence of these characteristic peaks in UPG aerogels verifies the successful incorporation of UiO-66-NH₂ into the PG aerogels.

Figure 4e,f illustrates the TGA curves and DTG curves of UiO-66-NH₂, PG aerogel, and UPG aerogels. The weight loss of the PG aerogel at nearly 100 °C was primarily caused by the evaporation of water from gelatin. The subsequent thermal decomposition stages involve the degradation of PLA and gelatin, as well as the gasification of their decomposition products [51]. For UiO-66-NH₂, three stages of weight loss were observed. Below 200 °C, the weight loss was associated with solvent evaporation. Between 200 and 300 °C, the second stage occurred due to the dihydroxylation of Zr₆O₄(OH)₄ clusters transforming into Zr₆O₆. Beyond 400 °C, the third stage corresponded to the decomposition of organic groups [42]. Notably, with the increase in the mass fraction of UiO-66-NH₂, the residual weight percentage of the aerogels exhibited a gradual upward trend. Calculations based on Equation (S1) show that the actual loading rates of UiO-66-NH₂ in UPG-5, UPG-10, UPG-15, and UPG-20 were 5.8 wt%, 9.8 wt%, 13.8 wt%, and 21.8 wt%, respectively, as detailed in Table S2. The percentage of UiO-66-NH₂ in the suspensions is lower than in the corresponding UPG aerogels, mainly due to the loss of PG fibers caused by the unstable structure of the aerogels during the freeze-drying process.

To examine the impact of UiO-66-NH₂ content on the pore structure of aerogels, N₂ adsorption–desorption experiments were conducted on UiO-66-NH₂ and a series of aerogels, as shown in Figure 4g–i and Table 2. The results revealed that UiO-66-NH₂ exhibits a high volume of micropores (Figure S4). In particular, as the UiO-66-NH₂ content increases, both the specific surface area and the micropore volume of the aerogels increase. The improvement in microporosity demonstrates that a higher UiO-66-NH₂ content effectively

enhances the pore structure of the aerogels, making them more suitable for use in gas adsorption and separation.

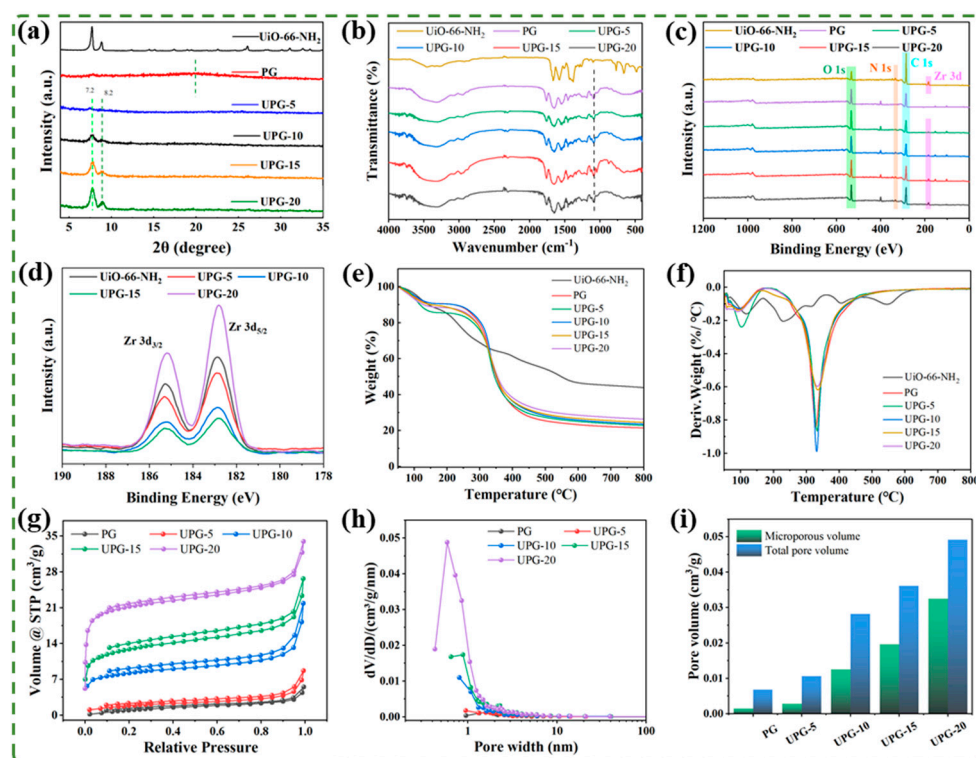


Figure 4. Characterization of the aerogels. (a) XRD, (b) FTIR, (c) XPS, (d) XPS spectra of Zr, (e) TGA, (f) DTG of the aerogels, (g) N₂ adsorption–desorption curves, (h) pore size distribution, and (i) pore volume of the different aerogels.

Table 2. Comparison of pore characteristics of the aerogels and UiO-66-NH₂ nanoparticles.

| Samples | Average Pore Diameter (nm) | BET Surface Area (m ² /g) |
|------------------------|----------------------------|--------------------------------------|
| PG | 5.48 | 5.55 |
| UPG-5 | 7.09 | 7.10 |
| UPG-10 | 4.32 | 30.08 |
| UPG-15 | 3.37 | 47.30 |
| UPG-20 | 2.52 | 81.26 |
| UiO-66-NH ₂ | 2.49 | 814.90 |

3.3. Air Purification Performance of the Aerogels

The air purification performance of the aerogels was comprehensively evaluated, focusing on PM, NH₃ adsorption, and DHC. In accordance with the air filtration standards (EN779:2012) [52], this study evaluated the filtration performance of the aerogels. The tests were conducted at a flow rate of 5.3 cm/s, using dust collected from animal farms as the target airborne particulate matter (PM). Figure 5a shows the filtration efficiencies and pressure drops for PG aerogel and UiO-66-NH₂-doped PG aerogels (UPG) at different concentrations. The results showed a similar trend in filtration efficiency across various particle sizes. Taking PM₁ as an example, the filtration efficiency and pressure drop gradually increased from PG to UPG-10, with UPG-10 achieving the highest filtration efficiency of 99.24% and a pressure drop of 95 Pa. In contrast, UPG-15 and UPG-20 exhibited reductions in both filtration efficiency and pressure drop. This decline may stem from the structural instability of the aerogel fibers caused by the addition of larger quantities of UiO-66-NH₂ nanoparticles. Notably, the UPG-10 exhibited the highest QF of 0.051 (for PM₁) compared

with other aerogels, as shown in Figure 5b. Moreover, compared with cylindrical fiber aerogel (PLA) and ribbon fiber aerogel (gelatin), the UPG-10 aerogel yielded the optimal filtration performance, as depicted in Figure 5c. This advantage is mainly attributed to the uniquely designed bionic “groove” ribbon fiber structure and the rougher surface caused by the UiO-66-NH₂ of the UPG-10 aerogel, making it more effective in capturing PM. In addition, the UPG-10 aerogel demonstrated a significant advantage in filtration performance compared to other reported filtration materials (Figure 5d). To further assess the stability of the UPG-10 aerogel in high-concentration particulate environments, a cyclic test was performed to remove dust with an initial concentration of approximately 1000 µg/m³. Over 20 repeated filtration cycles, the time required to reduce the particulate concentration to 50 µg/m³ remained nearly constant, demonstrating the exceptional stability and efficiency of UPG-10 aerogels in filtering high-concentration particulate matter, as illustrated in Figure 5e.

Figure 5f illustrates the NH₃ adsorption and desorption isotherms (at 25 °C) for both the PG aerogel and the UPG-10 aerogel. The maximum adsorption capacities of the PG aerogel and UPG-10 aerogel reached approximately 99.89 cm³/g and 68.43 cm³/g, respectively. This significant disparity in adsorption capacity is largely due to the integration of UiO-66-NH₂ nanoparticles into the UPG-10 aerogel. The addition of UiO-66-NH₂ substantially increased the specific surface area and pore volume of the aerogel, creating more active sites for NH₃ adsorption. Furthermore, the -NH₂ functional groups present in UiO-66-NH₂ were crucial in improving interactions with NH₃ by forming strong hydrogen bonds, as depicted in Figure 5g. This combination of an enlarged surface area and robust chemical interactions underscores the effectiveness of UiO-66-NH₂ in improving the NH₃ adsorption performance of the aerogels [53].

To better understand the advantages of three-dimensional aerogel structures in filtration applications, the structures of PG membranes and UPG-10 aerogels were analyzed. Figure 6a illustrates the overall layered distribution of the PG membrane, characterized by tightly packed fibers forming a dense structure. While this dense arrangement enhances particle capture, it may also result in higher pressure drop (Figure 6c). In contrast, Figure 6b reveals the three-dimensional porous fiber network structure of the UPG-10 aerogel, where the pores between fibers were significantly larger than those in the membrane. Due to the random distribution of fibers, particles repeatedly collide with fiber surfaces during their motion, and mutual collisions further alter their trajectories (Figure 6d). The filtration performance of the PG membrane and UPG-10 aerogel is shown in Figure 6e. While their filtration efficiencies for PM are similar, the UPG-10 aerogel demonstrates a 40 Pa lower pressure drop compared to the PG membrane, resulting in a higher quality factor (QF) for the aerogel, as shown in Figure 6f. This improved performance is primarily owing to the higher porosity and lower density of the UPG-10 aerogel (Figure 6g). The high porosity effectively reduces pressure drop, while the increased thickness ensures that the UPG-10 aerogel maintains high filtration efficiency, achieving superior overall filtration performance. Additionally, this structure greatly enhances the DHC of the UPG-10 aerogel. Figure 6h shows the filtration efficiency of PG aerogels and UPG-10 aerogels over a usage cycle, indicating that their filtration efficiencies did not differ significantly at different stages and gradually increased to nearly 100%. However, a significant difference was observed in their DHC. As shown in Figure 6i, UPG-10 aerogels exhibited an exceptional DHC of 147 g/m², which is three times higher than that of PG membranes. Furthermore, Figure 6j provides a comparison of the DHC of UPG-10 aerogels with other reported studies, highlighting their superior performance [10,17,28,31]. The UPG-10 aerogel exhibits a distinct advantage due to its excellent pore structure and high porosity, enabling a longer service life.

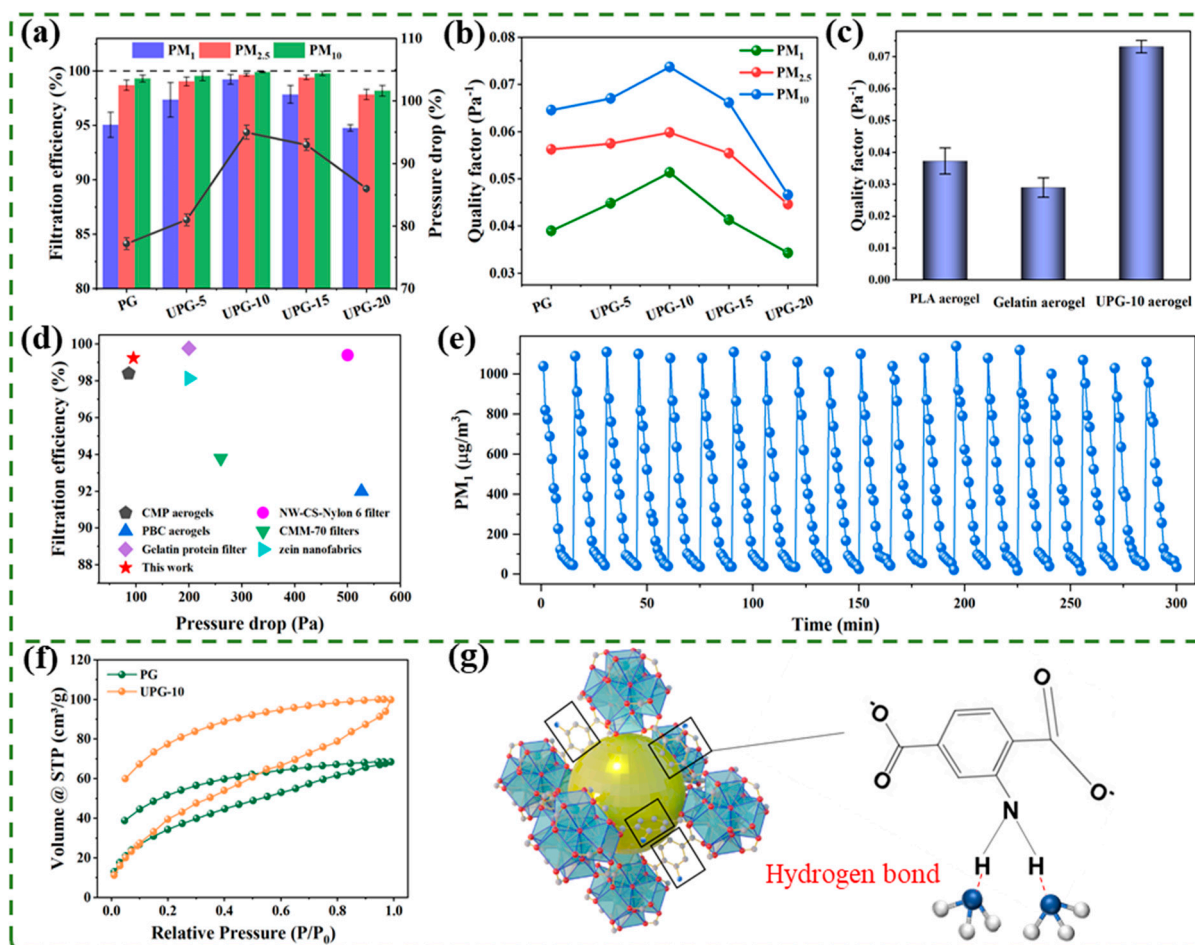


Figure 5. Air purification performance of the aerogels. (a) Filtration efficiency and pressure drop of the aerogels. (b) Quality factor of the aerogels. (c) Quality factor comparison among PLA aerogel, gelatin aerogel, and UPG-10 aerogel. (d) Comparison of the filtration performance of the UPG-10 aerogel with other reported filtration materials [11,54–58]. (e) Cyclic filtration test for PM_1 concentration variation over time. (f) The NH_3 adsorption isotherm of the PG aerogel and UPG-10 aerogel at 25 °C. (g) Schematic illustrating the adsorption of NH_3 by UiO-66- NH_2 via hydrogen bonding with its NH_2 groups.

3.4. Mechanical Performance of UPG-3 Aerogel

Good mechanical performance is crucial for an effective air filter. As shown in Figure 7a,b, UPG-10 aerogel exhibits high flexibility in both compression and bending tests, withstanding significant deformation and fully recovering its original shape. The compressive stress–strain curves at 20%, 40%, and 60% strain levels (Figure 7c) further highlight its excellent resilience under varying strains. The maximum stress exhibited a significant increase with strain, attaining values of 0.54 kPa at 20% strain and 1.75 kPa at 60% strain. Figure 7d presents the maximum compressive stress and plastic deformation across multiple compression cycles (1st, 10th, 20th, and 30th). With increasing cycles, the maximum compressive stress shows a slight decrease, while plastic deformation gradually increases. Even after 30 cycles, the aerogel maintains a high compressive stress level of 1.47 and recovers over 80% of its deformation, demonstrating strong fatigue resistance and elastic stability, as shown in Figure 7e. These properties highlight the potential of UPG-10 aerogel for air filtration applications. Figure 7f illustrates the elastic mechanism of the UPG-10 aerogel. When the aerogel is exposed to external compressive stress, individual nanofibers experience normal stress (F_1) perpendicular to the applied force. At the same time, adjacent fibers exhibit a tendency to move in opposing directions, leading to the

generation of shear forces (F_2) at their contact points. The superior elasticity of the aerogel is primarily attributed to these stable bonding points formed through high-temperature crosslinking. These bonding points play a crucial role by supporting the interconnections between nanofibers, enabling the network to maintain and recover its three-dimensional structure under applied stress. In contrast, the uncross-linked aerogels failed to recover after compression (Figure S5) due to the absence of cross-links, which rendered the nanofiber network incapable of sustaining the 3D structure under external forces.

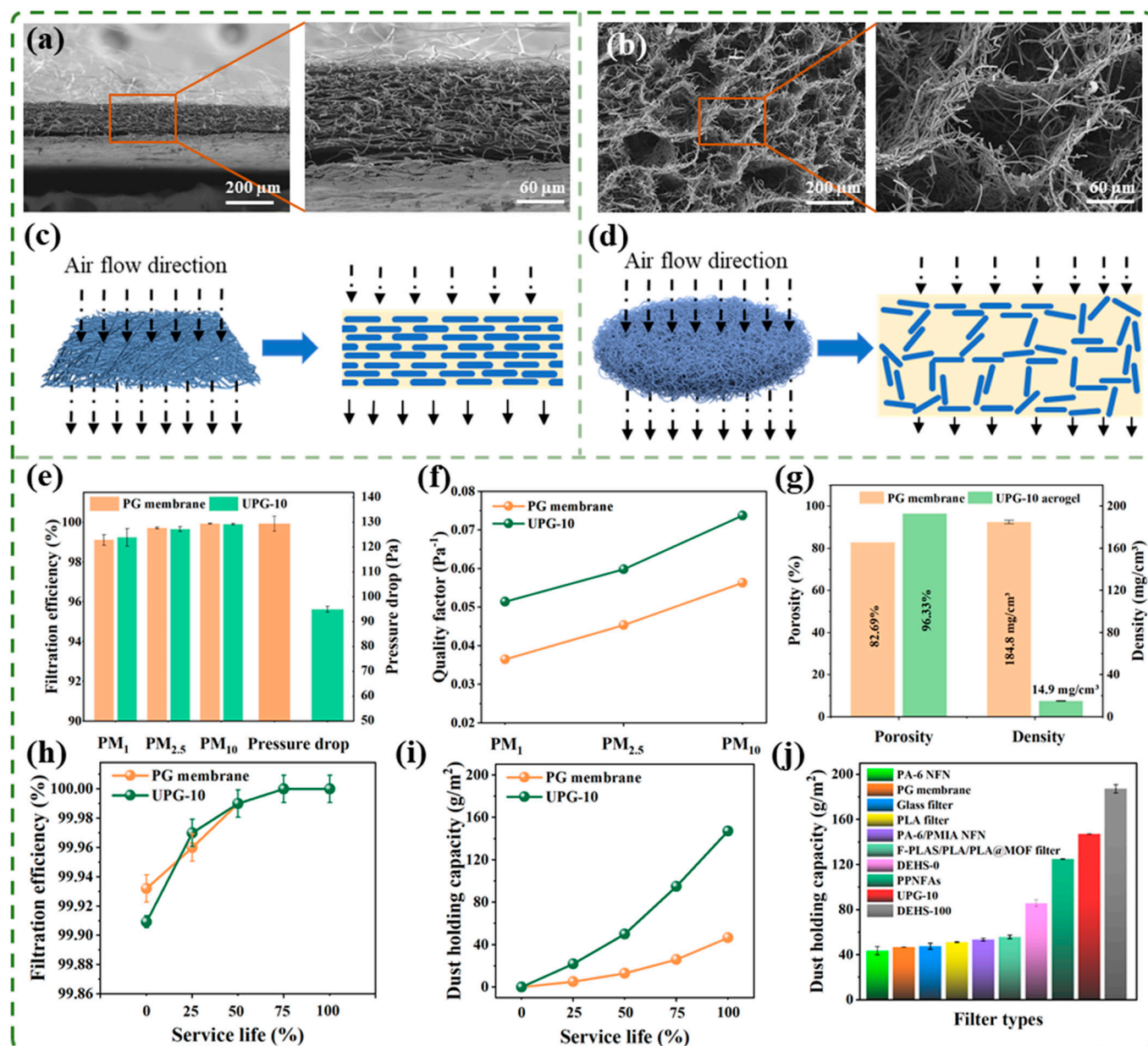


Figure 6. Comparison of the filtration performance between PG membrane and UPG-10 aerogel. SEM images and schematic diagram of the cross-section of (a,c) PG membrane and (b,d) UPG-10 aerogel. (e) Filtration efficiency, pressure drop, and (f) quality factor of PG membrane and UPG-10 aerogel for different particulate sizes. (g) Comparison of porosity and density of PG membrane and UPG-10 aerogel. (h) Filtration efficiency and (i) dust-holding capacity for PG Membrane and UPG-10 aerogel during a usage cycle. (j) Comparison of DHC between filtration materials prepared in this study with other reported studies [10,17,28,31].

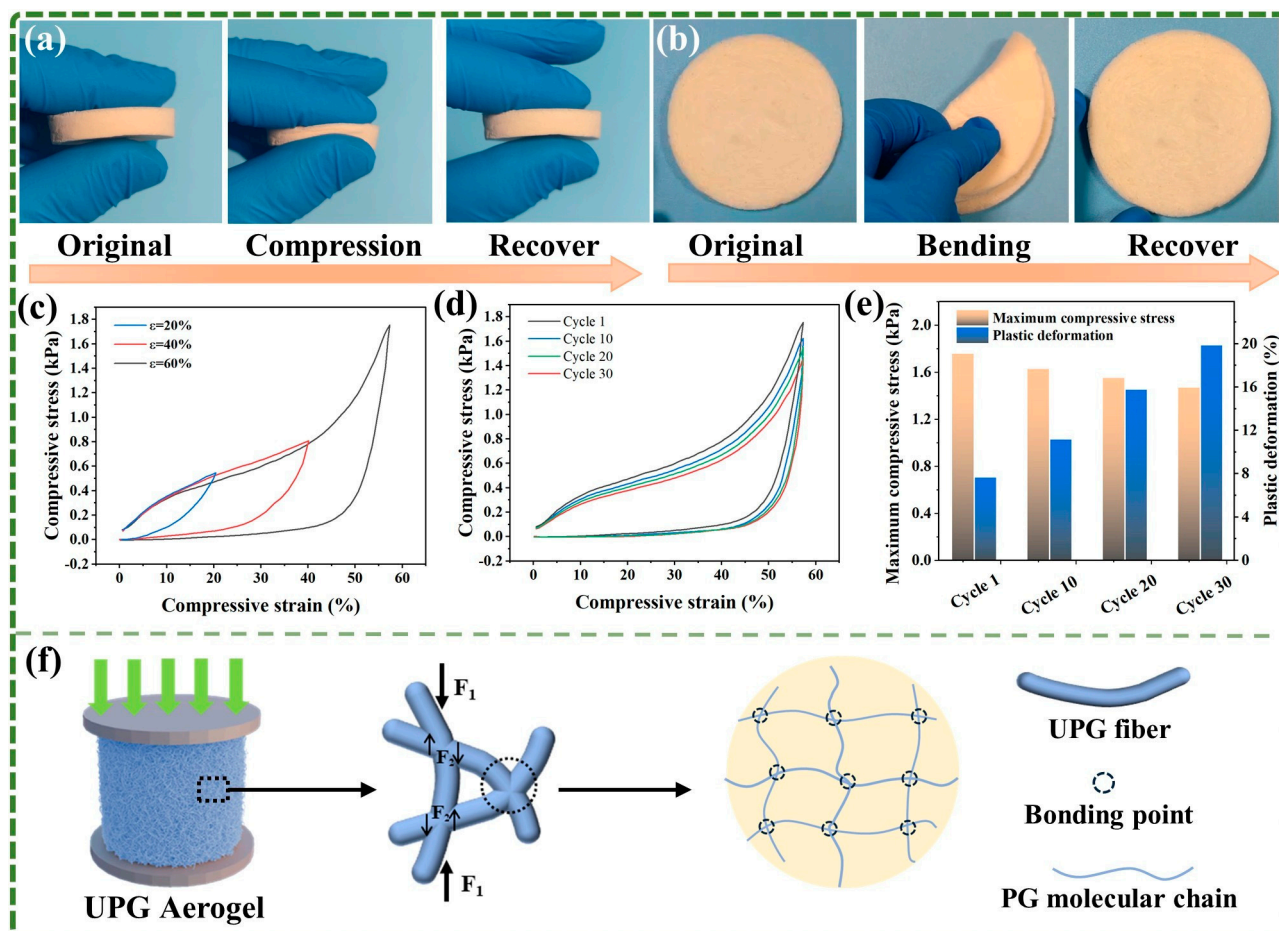


Figure 7. Mechanical properties and elastic mechanism of UPG-10 aerogel. High flexibility of UPG-10 aerogel demonstrated by (a) compressing test and (b) bending test. (c) Compressive stress–strain curves of the UPG-10 aerogel at different strains. (d) Compressive stress–strain curves under different compression cycles. (e) Maximum compressive stress and plastic deformation across compression cycles. (f) Schematic diagram of the internal stress conditions of UPG aerogel under the action of external force.

4. Conclusions

In this study, a high-performance biomimetic aerogel was developed, inspired by the dust-retention properties of *Pinus sylvestris* var. *mongolica* needles. By combining electro-spinning and freeze-forming technologies, we successfully fabricated a three-dimensional grooved ribbon-fiber aerogel incorporating UiO-66-NH₂ nanoparticles (UPG). This innovative design integrates structural advantages with functional enhancements, demonstrating outstanding filtration performance and mechanical stability. Among the various formulations evaluated, the UPG-10 aerogel achieved a filtration efficiency of 99.24% for PM₁ with a low pressure drop of 95 Pa, outperforming conventional PLA and gelatin aerogels. Its dust-holding capacity was three times higher than that of PG fiber membranes, ensuring an extended service life in high-concentration particle environments. The incorporation of UiO-66-NH₂ nanoparticles significantly enhanced NH₃ adsorption capacity through increased surface area and robust hydrogen bonding interactions, resulting in a 45.97% improvement compared to conventional PG aerogels. Additionally, mechanical evaluations demonstrated the excellent elasticity and resilience of the UPG-10 aerogel, retaining over 80% of its original shape after 30 compression cycles. Overall, the UPG-10 aerogel demonstrates a synergistic combination of high filtration efficiency, large dust-holding capacity, effective NH₃ adsorption, and mechanical robustness. These properties make

it a promising material for air purification, and offer insights for advancing biomimetic filtration technologies.

Supplementary Materials: The following supporting information can be downloaded at: <https://www.mdpi.com/article/10.3390/polym17091234/s1>, Equation (S1): Doping content of UiO-66-NH₂ in UPG-x; Figure S1: Test platform for assessing filtration performance; Figure S2: SEM of UiO-66-NH₂ nanoparticles; Figure S3: XPS spectra for the C, O, N, and Zr region of UPG-10 aerogel; Figure S4: Nitrogen adsorption–desorption isotherms (a) and pore size distribution (b) of UiO-66-NH₂; Figure S5: Non-heat-treated UPG aerogel demonstrated by (a) pressing test; Table S1: The elemental composition of the aerogels; Table S2: Composition of UPG-x.

Author Contributions: Methodology, B.Z., Z.H. and M.H.; software, Z.H.; formal analysis, B.Z.; resources, Q.W., Y.L. and X.L.; data curation, B.Z. and Z.H.; writing—original draft preparation, B.Z.; writing—review and editing, B.P., M.L., X.L., J.Q. and L.G.; visualization, Z.H.; supervision, J.Q. and L.G.; project administration, J.Q. and L.G.; funding acquisition, J.Q. and L.G. All authors have read and agreed to the published version of the manuscript.

Funding: This research was funded by the Research Foundation of Science and Technology Department of Jilin Province (Grant Nos. 20240304017SF) and the National Natural Science Foundation of China (Grant No. U23A6001).

Institutional Review Board Statement: Not applicable.

Informed Consent Statement: Not applicable.

Data Availability Statement: The original contributions presented in this study are included in the article. Further inquiries can be directed to the corresponding authors.

Acknowledgments: The authors thank Kaniki Tumba for his valuable comments and suggestions on the manuscript.

Conflicts of Interest: The authors declare no conflicts of interest.

References

1. Tang, Q.; Huang, K.; Liu, J.; Jin, X.; Li, C. Distribution Characteristics of Bioaerosols inside Pig Houses and the Respiratory Tract of Pigs. *Ecotoxicol. Environ. Saf.* **2021**, *212*, 112006. [\[CrossRef\]](#) [\[PubMed\]](#)
2. Khan, I.; Wang, W.; Ye, X.; Isa, A.M.; Khan, M.T.; Sa, R.; Liu, L.; Ma, T.; Zhang, H. Comparison of Bacterial Community Structure in PM_{2.5} within Broiler Houses under Different Rearing Systems in China. *Sustainability* **2022**, *14*, 1357. [\[CrossRef\]](#)
3. Wang, Y.; Li, W.; Gao, W.; Liu, Z.; Tian, S.; Shen, R.; Ji, D.; Wang, S.; Wang, L.; Tang, G.; et al. Trends in Particulate Matter and Its Chemical Compositions in China from 2013–2017. *Sci. China Earth Sci.* **2019**, *62*, 1857–1871. [\[CrossRef\]](#)
4. Zhang, Z.; Chai, P.; Wang, J.; Ye, Z.; Shen, P.; Lu, H.; Jin, M.; Gu, M.; Li, D.; Lin, H.; et al. Association of Particulate Matter Air Pollution and Hospital Visits for Respiratory Diseases: A Time-Series Study from China. *Environ. Sci. Pollut. Res.* **2019**, *26*, 12280–12287. [\[CrossRef\]](#)
5. Glendinning, L.; Collie, D.; Wright, S.; Rutherford, K.M.D.; McLachlan, G. Comparing Microbiotas in the Upper Aerodigestive and Lower Respiratory Tracts of Lambs. *Microbiome* **2017**, *5*, 145. [\[CrossRef\]](#) [\[PubMed\]](#)
6. Guo, L.; Zhao, B.; Jia, Y.; He, F.; Chen, W. Mitigation Strategies of Air Pollutants for Mechanical Ventilated Livestock and Poultry Housing—A Review. *Atmosphere* **2022**, *13*, 452. [\[CrossRef\]](#)
7. Li, P.; Wang, C.; Zhang, Y.; Wei, F. Air Filtration in the Free Molecular Flow Regime: A Review of High-Efficiency Particulate Air Filters Based on Carbon Nanotubes. *Small* **2014**, *10*, 4543–4561. [\[CrossRef\]](#)
8. Guo, J.; Xu, W.S.; Chen, Y.L.; Lua, A.C. Adsorption of NH₃ onto Activated Carbon Prepared from Palm Shells Impregnated with H₂SO₄. *J. Colloid Interface Sci.* **2005**, *281*, 285–290. [\[CrossRef\]](#)
9. Zhang, S.; Tang, N.; Cao, L.; Yin, X.; Yu, J.; Ding, B. Highly Integrated Polysulfone/Polyacrylonitrile/Polyamide-6 Air Filter for Multilevel Physical Sieving Airborne Particles. *ACS Appl. Mater. Interfaces* **2016**, *8*, 29062–29072. [\[CrossRef\]](#)
10. Zhang, S.; Liu, H.; Yu, J.; Luo, W.; Ding, B. Microwave Structured Polyamide-6 Nanofiber/Net Membrane with Embedded Poly(m-Phenylene Isophthalamide) Staple Fibers for Effective Ultrafine Particle Filtration. *J. Mater. Chem. A* **2016**, *4*, 6149–6157. [\[CrossRef\]](#)
11. Tian, H.; Fu, X.; Zheng, M.; Wang, Y.; Li, Y.; Xiang, A.; Zhong, W.-H. Natural Polypeptides Treat Pollution Complex: Moisture-Resistant Multi-Functional Protein Nanofabrics for Sustainable Air Filtration. *Nano Res.* **2018**, *11*, 4265–4277. [\[CrossRef\]](#)

12. Li, Y.; Cao, L.; Yin, X.; Si, Y.; Yu, J.; Ding, B. Semi-Interpenetrating Polymer Network Biomimetic Structure Enables Superelastic and Thermostable Nanofibrous Aerogels for Cascade Filtration of PM_{2.5}. *Adv. Funct. Mater.* **2020**, *30*, 1910426. [\[CrossRef\]](#)
13. Zhang, T.; Yin, L.; Wang, X.; Fu, H.; Li, Y.; Zhang, D.; Huang, J.; Qian, X.; Lai, Y.; Zhang, S. Robust Three-Dimensional Bioinspired Honeycomb Structured Ultra-Elastic Aerogels for High-Temperature Cascade Filtration Applications. *J. Clean. Prod.* **2024**, *442*, 141014. [\[CrossRef\]](#)
14. Cao, L.; Wang, C.; Huang, Y. Structure Optimization of Graphene Aerogel-Based Composites and Applications in Batteries and Supercapacitors. *Chem. Eng. J.* **2023**, *454*, 140094. [\[CrossRef\]](#)
15. Qiao, S.; Zhang, H.; Kang, S.; Quan, J.; Hu, Z.; Yu, J.; Wang, Y.; Zhu, J. Hydrophobic, Pore-Tunable Polyimide/Polyvinylidene Fluoride Composite Aerogels for Effective Airborne Particle Filtration. *Macromol. Mater. Eng.* **2020**, *305*, 2000129. [\[CrossRef\]](#)
16. Su, Q.; Zhu, C.; Gong, A.; Long, S.; Zhang, G.; Wei, Z.; Wang, X.; Yang, J. Novel Multi-Hierarchical Nanofiber Aerogel for High Efficient Filtration of High-Temperature Flue Gas. *Sep. Purif. Technol.* **2024**, *347*, 127573. [\[CrossRef\]](#)
17. Yue, W.; Cao, Y.; Han, R.; Ren, L.; Liu, S.; Liu, F.; He, J.; Shao, W.; Chen, L. A Synergistic Strategy for Fabricating a Highly Flexible Poly(M-phenylene Isophthalamide) Nanofiber-reinforced Polyimide Aerogel for High-temperature Filtration. *J. Appl. Polym. Sci.* **2023**, *140*, e54705. [\[CrossRef\]](#)
18. Strain, I.N.; Wu, Q.; Pourrahimi, A.M.; Hedenqvist, M.S.; Olsson, R.T.; Andersson, R.L. Electrospinning of Recycled PET to Generate Tough Mesomorphic Fibre Membranes for Smoke Filtration. *J. Mater. Chem. A* **2015**, *3*, 1632–1640. [\[CrossRef\]](#)
19. Zhang, W.; Huang, T.; Ren, Y.; Wang, Y.; Yu, R.; Wang, J.; Tu, Q. Preparation of Chitosan Crosslinked with Metal-Organic Framework (MOF-199)@aminated Graphene Oxide Aerogel for the Adsorption of Formaldehyde Gas and Methyl Orange. *Int. J. Biol. Macromol.* **2021**, *193*, 2243–2251. [\[CrossRef\]](#)
20. Shang, M.; Peng, X.; Zhang, J.; Liu, X.; Yuan, Z.; Zhao, X.; Liu, S.; Yu, S.; Yi, X.; Filatov, S. Sodium Alginate-Based Carbon Aerogel-Supported ZIF-8-Derived Porous Carbon as an Effective Adsorbent for Methane Gas. *ACS Appl. Mater. Interfaces* **2023**, *15*, 14634–14642. [\[CrossRef\]](#)
21. Liu, Y.; Yu, B.; Chen, X.; Li, D.; Zhou, C.; Guo, Z.-R.; Xu, W.; Yang, S.; Zhang, J. One-Droplet Synthesis of Polysaccharide/Metal-Organic Framework Aerogels for Gas Adsorption. *ACS Appl. Polym. Mater.* **2023**, *5*, 4327–4332. [\[CrossRef\]](#)
22. Feng, Y.; Zhang, M.; Sun, Y.; Cao, C.; Wang, J.; Ge, M.; Cai, W.; Mi, J.; Lai, Y. Porous Carbon Nanofibers Supported Zn/MnO Sorbents with High Dispersion and Loading Content for Hot Coal Gas Desulfurization. *Chem. Eng. J.* **2023**, *464*, 142590. [\[CrossRef\]](#)
23. Feng, Y.; Wang, J.; Hu, Y.; Lu, J.; Zhang, M.; Mi, J. Microwave Heating Motivated Performance Promotion and Kinetic Study of Iron Oxide Sorbent for Coal Gas Desulfurization. *Fuel* **2020**, *267*, 117215. [\[CrossRef\]](#)
24. Ru, Z.; Zhang, X.; Zhang, M.; Mi, J.; Cao, C.; Yan, Z.; Ge, M.; Liu, H.; Wang, J.; Zhang, W.; et al. Bimetallic-MOF-Derived Zn_xCo_{3-x}O₄/Carbon Nanofiber Composites Sorbents for High-Temperature Coal Gas Desulfurization. *Environ. Sci. Technol.* **2022**, *56*, 17288–17297. [\[CrossRef\]](#) [\[PubMed\]](#)
25. Jasuja, H.; Peterson, G.W.; Decoste, J.B.; Browe, M.A.; Walton, K.S. Evaluation of MOFs for Air Purification and Air Quality Control Applications: Ammonia Removal from Air. *Chem. Eng. Sci.* **2015**, *124*, 118–124. [\[CrossRef\]](#)
26. Song, Y.; Chau, J.; Sirkar, K.K.; Peterson, G.W.; Beuscher, U. Membrane-Supported Metal Organic Framework Based Nanopacked Bed for Protection against Toxic Vapors and Gases. *Sep. Purif. Technol.* **2020**, *251*, 117406. [\[CrossRef\]](#)
27. Garibay, S.J.; Cohen, S.M. Isoreticular Synthesis and Modification of Frameworks with the UiO-66 Topology. *Chem. Commun.* **2010**, *46*, 7700. [\[CrossRef\]](#)
28. Zhao, B.; Han, M.; Wang, Q.; Huang, Z.; Liang, Y.; Tumba, K.; Li, M.; Chen, W.; Kamal, M.; Chang, Z.; et al. Polylactic Acid-Based Composite Filter with Multi-Gradient Structure Developed for High-Efficiency Particulate Matter Filtration and NH₃ Purification. *Sep. Purif. Technol.* **2025**, *354*, 129354. [\[CrossRef\]](#)
29. Liu, S.; Huang, Q.; Chen, C.; Song, Y.; Zhang, X.; Dong, W.; Zhang, W.; Zhao, B.; Nan, B.; Zhang, J.; et al. Joint Effect of Indoor Size-Fractioned Particulate Matters and Black Carbon on Cardiopulmonary Function and Relevant Metabolic Mechanism: A Panel Study among School Children. *Environ. Pollut.* **2022**, *307*, 119533. [\[CrossRef\]](#)
30. Kaur, S.; Sundararajan, S.; Rana, D.; Sridhar, R.; Gopal, R.; Matsuura, T.; Ramakrishna, S. Review: The Characterization of Electrospun Nanofibrous Liquid Filtration Membranes. *J. Mater. Sci.* **2014**, *49*, 6143–6159. [\[CrossRef\]](#)
31. Yao, Y.; Liu, S.; You, T.; Zhou, Z.; Zhang, X.; Tang, M.; Sun, Z.; Wang, J.; Hu, J. Application of Microfibrillated Fibers in Robust and Reusable Air Filters with Long Service Time in the Ambient with High Oily Aerosols Concentration. *Sep. Purif. Technol.* **2022**, *295*, 121263. [\[CrossRef\]](#)
32. Liu, H.; Zhang, S.; Liu, L.; Yu, J.; Ding, B. High-Performance Filters from Biomimetic Wet-Adhesive Nanoarchitected Networks. *J. Mater. Chem. A* **2020**, *8*, 18955–18962. [\[CrossRef\]](#)
33. Deng, Y.; Lu, T.; Zhang, X.; Zeng, Z.; Tao, R.; Qu, Q.; Zhang, Y.; Zhu, M.; Xiong, R.; Huang, C. Multi-Hierarchical Nanofiber Membrane with Typical Curved-Ribbon Structure Fabricated by Green Electrospinning for Efficient, Breathable and Sustainable Air Filtration. *J. Membr. Sci.* **2022**, *660*, 120857. [\[CrossRef\]](#)
34. Guo, L.; Zhao, B.; Zhao, D.; Li, J.; Tong, J.; Chang, Z.; Liu, X. Evaluation of Conifer and Broad-Leaved Barriers in Intercepting Particulate Matters in a Wind Tunnel. *J. Air Waste Manag. Assoc.* **2020**, *70*, 1314–1323. [\[CrossRef\]](#) [\[PubMed\]](#)

35. Mann-Lahav, M.; Halabi, M.; Shter, G.E.; Beilin, V.; Balaish, M.; Ein-Eli, Y.; Dekel, D.R.; Grader, G.S. Electrospun Ionomeric Fibers with Anion Conducting Properties. *Adv. Funct. Mater.* **2020**, *30*, 1901733. [\[CrossRef\]](#)
36. Li, Y.; Hua, Y.; Ji, Z.; Wu, Z.; Fan, J.; Liu, Y. Dual-Bionic Nano-Groove Structured Nanofibers for Breathable and Moisture-Wicking Protective Respirators. *J. Membr. Sci.* **2023**, *672*, 121257. [\[CrossRef\]](#)
37. Topuz, F.; Uyar, T. Electrospinning of Gelatin with Tunable Fiber Morphology from Round to Flat/Ribbon. *Mater. Sci. Eng. C* **2017**, *80*, 371–378. [\[CrossRef\]](#) [\[PubMed\]](#)
38. Wang, C.; Hashimoto, T. A Scenario of a Fiber Formation Mechanism in Electrospinning: Jet Evolves Assemblies of Phase-Separated Strings That Eventually Split into As-Spun Fibers Observed on the Grounded Collector. *Macromolecules* **2020**, *53*, 9584–9600. [\[CrossRef\]](#)
39. Li, H.; Zhu, L.; Zhang, J.; Guo, T.; Li, X.; Xing, W.; Xue, Q. High-Efficiency Separation Performance of Oil-Water Emulsions of Polyacrylonitrile Nanofibrous Membrane Decorated with Metal-Organic Frameworks. *Appl. Surf. Sci.* **2019**, *476*, 61–69. [\[CrossRef\]](#)
40. Schaate, A.; Roy, P.; Godt, A.; Lippke, J.; Waltz, F.; Wiebcke, M.; Behrens, P. Modulated Synthesis of Zr-Based Metal-Organic Frameworks: From Nano to Single Crystals. *Chem. Eur. J.* **2011**, *17*, 6643–6651. [\[CrossRef\]](#)
41. Wu, D.-Y.; Wang, S.-S.; Wu, C.-S. Antibacterial Properties and Cytocompatibility of Biobased Nanofibers of Fish Scale Gelatine, Modified Polylactide, and Freshwater Clam Shell. *Int. J. Biol. Macromol.* **2020**, *165*, 1219–1228. [\[CrossRef\]](#) [\[PubMed\]](#)
42. Pang, J.; Sun, Q.; Guo, Z.; Guo, H.; Guo, X.; Huang, J.; Shang, Y.; Zeng, J.; Kang, Z. Electrospinning UiO-66-NH₂/Polyacrylonitrile Fibers for Filtration of VOCs. *Micropor. Mesopor. Mat.* **2022**, *343*, 112167. [\[CrossRef\]](#)
43. Mozafari, M.; Abedini, R.; Rahimpour, A. Zr-MOFs-Incorporated Thin Film Nanocomposite Pebax 1657 Membranes Dip-Coated on Polymethylpentylene Layer for Efficient Separation of CO₂/CH₄. *J. Mater. Chem. A* **2018**, *6*, 12380–12392. [\[CrossRef\]](#)
44. Khatami, F.; Baharian, A.; Akbari-Birgani, S.; Nikfarjam, N. Tubular Scaffold Made by Gelatin/Polylactic Acid Nanofibers for Breast Ductal Carcinoma in Situ Tumor Modeling. *J. Drug Deliv. Sci. Technol.* **2023**, *85*, 104606. [\[CrossRef\]](#)
45. Bakeshlou, Z.; Nikfarjam, N. Thermoregulating Papers Containing Fabricated Microencapsulated Phase Change Materials through Pickering Emulsion Templating. *Ind. Eng. Chem. Res.* **2020**, *59*, 20253–20268. [\[CrossRef\]](#)
46. Liu, J.; Lin, S.; Dang, J.; Wang, S.; Cheng, W.; Ran, Z.; Zhu, H.; Deng, H.; Xiong, C.; Xu, W.; et al. Anticancer and Bone-Enhanced Nano-Hydroxyapatite/Gelatin/Polylactic Acid Fibrous Membrane with Dual Drug Delivery and Sequential Release for Osteosarcoma. *Int. J. Biol. Macromol.* **2023**, *240*, 124406. [\[CrossRef\]](#)
47. Pan, J.; Wang, L.; Shi, Y.; Li, L.; Xu, Z.; Sun, H.; Guo, F.; Shi, W. Construction of Nanodiamonds/UiO-66-NH₂ Heterojunction for Boosted Visible-Light Photocatalytic Degradation of Antibiotics. *Sep. Purif. Technol.* **2022**, *284*, 120270. [\[CrossRef\]](#)
48. Yuan, W.; Li, S.; Guan, H.; Zhang, S.; Zhang, Y.; Zhang, M.; Yu, Y.; Chen, X. Preparation and Properties of a Novel Biodegradable Composite Hydrogel Derived from Gelatin/Chitosan and Polylactic Acid as Slow-Release N Fertilizer. *Polymers* **2023**, *15*, 997. [\[CrossRef\]](#)
49. Lv, S.-W.; Liu, J.-M.; Li, C.-Y.; Zhao, N.; Wang, Z.-H.; Wang, S. In Situ Growth of Benzothiadiazole Functionalized UiO-66-NH₂ on Carboxyl Modified g-C₃N₄ for Enhanced Photocatalytic Degradation of Sulfamethoxazole under Visible Light. *Catal. Sci. Technol.* **2020**, *10*, 4703–4711. [\[CrossRef\]](#)
50. Yang, X.; Xu, Q.; Yan, N.; Sui, G.; Cai, Q.; Deng, X. Structure and Wettability Relationship of Coelectrospun Poly(L-lactic Acid)/Gelatin Composite Fibrous Mats. *Polym. Adv. Technol.* **2011**, *22*, 2222–2230. [\[CrossRef\]](#)
51. Alippilakkotte, S.; Sreejith, L. Benign Route for the Modification and Characterization of Poly(Lactic Acid) (PLA) Scaffolds for Medicinal Application. *J. Appl. Polym. Sci.* **2018**, *135*, 46056. [\[CrossRef\]](#)
52. CEN.EN 779:2012; Particulate Air Filters for General Ventilation—Determination of the Filtration Performance. European Committee for Standardization (CEN): Brussels, Belgium, 2012.
53. Kim, K.C.; Yu, D.; Snurr, R.Q. Computational Screening of Functional Groups for Ammonia Capture in Metal–Organic Frameworks. *Langmuir* **2013**, *29*, 1446–1456. [\[CrossRef\]](#) [\[PubMed\]](#)
54. Fu, Q.; Liu, Y.; Liu, T.; Mo, J.; Zhang, W.; Zhang, S.; Luo, B.; Wang, J.; Qin, Y.; Wang, S.; et al. Air-Permeable Cellulosic Triboelectric Materials for Self-Powered Healthcare Products. *Nano Energy* **2022**, *102*, 107739. [\[CrossRef\]](#)
55. Xiong, Z.; Li, X.; Wang, J.; Lin, J. Nanocellulose Implantation Enriched the Pore Structure of Aerogel for Effective Particulate Matter Removal. *Int. J. Biol. Macromol.* **2022**, *219*, 1237–1243. [\[CrossRef\]](#)
56. Li, H.; Wang, T.; Ying, Y.; Wang, Z.; Pan, L.; Wang, S. Hierarchical Cu-MOF Hollow Nanowire Modified Copper Mesh for Efficient Antibacterial PM Filtration. *Inorg. Chem. Front.* **2023**, *10*, 2457–2465. [\[CrossRef\]](#)

57. Xiong, F.; Wang, X.; Liu, Y.; Zhang, Z.; Zhang, T.; Gao, H.; Fu, H.; Huang, J.; Qian, X.; Lai, Y.; et al. Sandwich Structured Chitosan-Aerogel Nonwoven Filter with Asymmetric Wettability and Pore Size Differences for High-Efficient Oil-Mist Filtration. *J. Environ. Chem. Eng.* **2023**, *11*, 110443. [\[CrossRef\]](#)
58. Souzandeh, H.; Wang, Y.; Zhong, W.-H. “Green” Nano-Filters: Fine Nanofibers of Natural Protein for High Efficiency Filtration of Particulate Pollutants and Toxic Gases. *RSC Adv.* **2016**, *6*, 105948–105956. [\[CrossRef\]](#)

Disclaimer/Publisher’s Note: The statements, opinions and data contained in all publications are solely those of the individual author(s) and contributor(s) and not of MDPI and/or the editor(s). MDPI and/or the editor(s) disclaim responsibility for any injury to people or property resulting from any ideas, methods, instructions or products referred to in the content.